

Temperature-Dependent Minority-Carrier Mobility in *p*-Type InAs/GaSb Type-II-Superlattice Photodetectors

Z. Taghipour,^{1,2,*} S. Lee,² S.A. Myers,³ E.H. Steenberg,⁴ C.P. Morath,⁴ V.M. Cowan,⁴ S. Mathews,² G. Balakrishnan,⁵ and S. Krishna^{2,†}


¹Center for High Technology Materials, University of New Mexico, New Mexico 87106, USA

²Department of Electrical and Computer Engineering, The Ohio State University, Ohio 43210, USA

³SK Infrared LLC, Columbus, Ohio 43210, USA

⁴Air Force Research Laboratory, Kirtland Air Force Base, New Mexico 87108, USA

⁵Department of Electrical and Computer Engineering, University of New Mexico, New Mexico 87106, USA

 (Received 18 July 2018; revised manuscript received 15 December 2018; published 19 February 2019)

Infrared (IR) detectors and focal-plane arrays based on superlattices have progressed significantly during the past decade. However, there are still fundamental challenges associated with this system, especially in understanding the transport of minority carriers due to the anisotropy in the band structure and the quantum-confined miniband transport. In this paper, we investigate the key parameters influencing the vertical minority-electron transport and lifetime in *nBp* midwave infrared (MWIR) detectors with a *p*-type InAs/GaSb type-II-superlattice (T2SL) absorber. We measure the minority carrier diffusion length using the temperature-dependent electron-beam-induced-current (EBIC) method at three electron-beam (*e*-beam) energies. Our results show that the diffusion length is independent of the temperature from 80 to 140 K and increases linearly beyond that. By varying the *e*-beam energies and the beam current in EBIC, we examine the effect of carrier distributions from the surface in our measurement. We further study the minority-carrier lifetime using the time-resolved-microwave-reflectance (TMR) measurement as a function of the temperature and the excitation density. The TMR results indicate that the lifetime is Shockley-Read-Hall (SRH) limited for the temperature range of interest in this work (80–150 K) and the Auger recombination is dominant above 150 K, while the radiative recombination is negligible. The combined results of the diffusion length and the lifetime are used to determine the temperature-dependent mobility along the growth direction. The transport is found to be limited by deep-level states for temperatures below 140 K and the activation energy of 115 meV is calculated from the minority-carrier mobility results for temperatures above 140 K. This effort is a theoretical and experimental study to address some of the essential questions regarding the transport in InAs/GaSb T2SLs, the result of which would help optimize the design and growth of T2SL structures with improved performance.

DOI: [10.1103/PhysRevApplied.11.024047](https://doi.org/10.1103/PhysRevApplied.11.024047)

I. INTRODUCTION

The past decade has witnessed a dramatic improvement in the performance of infrared detectors and focal-plane arrays (FPAs) based on type-II superlattices [1]. There are reports of commercial infrared cameras based on antimonide superlattices [2,3]. However, there is still a lack of understanding of the transport of carriers in this material system. The complications arise from the fact that the conduction properties of superlattices are highly anisotropic due to the quasi-two-dimensional-(2D)-three-dimensional (3D) nature of the density of states. This anisotropy is imposed by the degree of quantum confinement as a result

of numerous repeats of a few nanometer-thick alternate layers of InAs and GaSb and the type-II band alignment [4]. The highly anisotropic nature of the band structure and the modified density of states leads to transport that is very different from bulk-isotropic systems such as InSb and (Hg,Cd)Te, which has been the traditional workhorse material for the infrared-detector community [5]. To improve the performance of photodiodes based on the narrow-band-gap T2SL materials, knowledge of the minority-carrier transport and its limitations is necessary. The work in this paper is centered around understanding the transport of carriers using the measurement of the minority-carrier diffusion length and lifetime.

In general, the drift and diffusion of excess electrons and holes, defined via the ambipolar mobility μ or the diffusion coefficient D , are used to explain the transport behavior of

*taghipour.5@osu.edu

†krishna.53@osu.edu

excess carriers generated in a semiconductor device. It is not always known to what extent both diffusion and drift are involved in charge movements, unless we know that only one of these mechanisms prevails. The carrier drift mobility and diffusion coefficient are related through the Einstein relation as

$$D = \frac{k_B T \mu}{q}, \quad (1)$$

where k_B is Planck's constant, T is the temperature, and q is the fundamental charge of an electron. This relation is valid under the thermal-equilibrium condition [6]. Nevertheless, it can be used as an approximation to extract the drift mobility, if the diffusion coefficient is known. Diffusion is further dependent on an average distance that the relevant charge moves in the semiconductor before its recombination and/or extraction from it and hence is related to the minority-carrier diffusion length (L_{MC}) and the minority-carrier lifetime (τ_{MC}) through $L_{MC} = \sqrt{D\tau_{MC}}$. So, if one performs an independent lifetime characterization along with the diffusion-length measurement, the diffusion coefficient and, subsequently, the carrier mobility can be determined.

Superlattice vertical transport properties are typically interrogated using vertical magnetotransport measurement [7], the ultrafast all-optical time-of-flight technique [8], or the e -beam-induced-microscopy method [9–12]. Among previous studies, there are few available experimental transport data on p -type T2SL photodetectors. One study, by Li *et al.*, reports on the diffusion length of minority electrons in a long-wave infrared (LWIR) p - i - n T2SL structure and extracts the minority-carrier lifetime using previously reported mobility values [9]. Umana-Membreno *et al.* have investigated the vertical minority-electron mobility in a LWIR T2SL structure using the magnetotransport method [7]. Transport in p -type midwave infrared (MWIR) T2SL structures has also been reported through the application of the quantum-efficiency modeling technique [13] and as a means of investigation of the gamma-irradiation effect [12].

Short carrier lifetimes in T2SLs, limited by Shockley-Read-Hall (SRH) centers, mandate the use of barrier architectures for operation at elevated temperatures [14]. Therefore, photodetector architectures utilizing wide-band-gap barriers are the current state of the art, due to their higher collection efficiency of photogenerated carriers and reduced dark-current generation without inhibiting photocurrent [15,16]. Among barrier architectures, nBn vertical photoconductors with n -type absorbers and electron barriers have shown much promise due to their low thermal generation and surface leakage about the junction [17]. In the nBp variant of this design, used for this study, the n -type absorber is replaced by a p -doped layer and the electron barrier is replaced with a hole barrier. Unlike the

nBn , in which the operation is similar to a photoconductor that requires an applied bias, the nBp is a photodiode with a built-in potential that can operate with zero applied bias [18,19].

In this work, we undertake a comprehensive study to extract the critical transport parameters and minority lifetime in a nBp MWIR detector with a p -type ten-monolayer (10 ML) InAs/10 ML GaSb T2SL absorber. We study the temperature- and excess-density-dependence of the minority-carrier lifetime using time-resolved-microwave-reflectance (TMR) measurements. We also investigate the contributions of the various recombination mechanisms, such as SRH, radiative, and Auger recombination, as a function of the temperature and the excess carrier density to provide greater insight into the nonequilibrium carrier dynamics in the photodetector. Furthermore, we use the electron-beam-induced-current (EBIC) method to measure the carrier diffusion length on the processed T2SL photodetector sample. Finally, we extract the minority-carrier mobility in the growth direction using the results for L_{MC} and τ_{MC} as a function of the temperature.

The proposed study seeks to be among the continuing efforts to improve T2SL IR detectors performance by gaining a physical insight into these materials. Ultimately, the results can be used to optimize the design and growth of T2SL structures with improved transport, which in turn will lead to the realization of IR photodetectors with enhanced performance.

This paper is organized as follows. Section II reviews the sample design used for this work. Section III presents the experimental approach used for measuring the minority-carrier lifetime and the analytical modeling to study the limiting mechanism in the carrier recombination as a function of the temperature and the excess density. Section IV discusses the experimental details of the EBIC measurement and the semiparametric modeling technique used for extracting the diffusion length. Section V summarizes the critical observations and discusses the minority-carrier mobility as a function of the temperature. Finally, Sec. VI concludes with the main observation points.

II. SAMPLE AND METHOD

The nBp MWIR T2SL structure is grown by solid-source molecular-beam epitaxy on a tellurium-doped GaSb(001) epitaxial substrate. The epilayer consists of a 250-nm nonintentionally doped GaSb buffer layer, followed by a 1.5- μ m-thick p -doped ($5 \times 10^{17} \text{ cm}^{-3}$) bottom contact layer. The absorber consists of a 4- μ m-thick p -doped ($5 \times 10^{16} \text{ cm}^{-3}$) layer. Both the bottom contact and the absorber are composed of a 10 ML InAs/10 ML GaSb T2SL with a band gap of 0.250 eV at 77 K. A 250-nm-thick lightly n -doped ($5 \times 10^{15} \text{ cm}^{-3}$) hole barrier with a band gap of 0.5 eV composed of a 12 ML InAs/6 ML AlSb T2SL is then grown. Lastly, the growth is followed

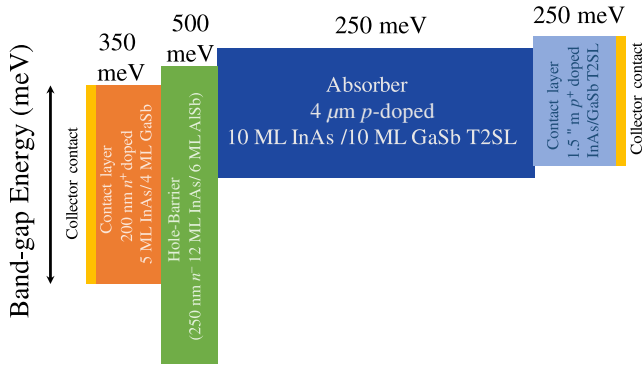


FIG. 1. The relative band gap of the nBp InAs/GaSb T2SL photodetector, showing the thickness of each constituent layer. The band gaps are calculated from the simulation of Naval Research Laboratory NRL MULTIBANDS[®] software at 77 K. The layer thicknesses are not drawn to scale.

by a 200-nm-thick n -doped ($5 \times 10^{17} \text{ cm}^{-3}$) top contact layer with a band gap of 0.350 eV, composed of a 5 ML InAs/4 ML GaSb T2SL. The band-edge energy diagram is illustrated in Fig. 1.

The epilayer is then processed into variable-area single-pixel devices using standard fabrication techniques. The shallow-etch scheme is incorporated during device fabrication such that the pixel mesas are defined down to the wide-band-gap material and not to the bottom contact layer. These pixels are then metalized, wire-bonded, and packaged for further electrical characterizations.

In order to extract information about the minority-carrier mobility (μ_e) in this sample, we use the Einstein relation, written in terms of the minority diffusion length L_e and the minority-carrier lifetime τ_e as

$$\mu_e = \frac{q}{k_B T} \frac{L_e^2}{\tau_e}. \quad (2)$$

We measure τ_e and L_e using TMR and EBIC, respectively. The following section will review the experimental details and theoretical platform used to extract the minority-carrier lifetime and investigate various limiting recombination mechanisms.

III. LIFETIME CHARACTERIZATION

A. Experimental measurement

The lifetime measurement setup based on TMR utilizes a pulsed laser to excite electron-hole pairs in the semiconductor material. The generation of excess charges and the subsequent recombination processes alter the conductivity, which in turn changes the reflection of continuous-wave microwave radiation from the sample. By temporally monitoring the power of the reflected microwave signal after optical excitation, one can extract the recombination rate and hence estimate the carrier's lifetime.

For this work, we use a 1535-nm pulsed laser with about a 5-ns full-width-at-half-maximum pulse width, a 2.5-kHz repetition rate, and a beam-spot-size diameter of 0.1 cm to inject the excess carriers. A micro-electromechanical-(MEMs-) based modulator is used to adjust the excitation fluence from 0.5 to $74 \mu\text{J cm}^{-2}$. The reflected TMR signal is then amplified using a preamplifier with a 200 MHz bandwidth and detected using a high-resolution (12-bit) and high-speed [10 GS/s (gigasamples per second)] digitizer.

We etch an unprocessed portion of the T2SL photodetector wafer down to the absorber layer to accurately measure the nonequilibrium carrier dynamics without the effects of the contact and barrier layers. The sample is then mounted in a cryostat coupled with a temperature controller and the lifetime characterization is repeated for temperatures between 20 K and room temperature. In order to estimate the injected carrier density in the sample, the absorption coefficient is calculated using previously reported value of a 3500-nm penetration depth for the same optical excitation energy in a similar superlattice material [20].

Figure 2 shows the obtained results for a subset of injected carrier densities and temperatures. The results indicate an initial decay during the first 200 ns following the generation of excess carriers. In addition, a secondary decay is observed for temperatures up to 200 K for excitation levels above $1.0 \times 10^{17} \text{ cm}^{-3}$ and up to 150 K for the lower excitation levels, and becomes less distinctive as the incident pump fluence or the initial excess carrier is decreased. The first decay is associated with the recombination of carriers upon generation, whereas the secondary decay is not usually observed and its origin is unknown to us. While further investigation is currently under way regarding this observation, we hypothesize that this secondary decay might be due to the presence of defects and is originated through the band-to-deep-level-state recombination.

For the purpose of this work, we focus on the first decay to extract the minority-carrier lifetime. We have used analytical modeling to determine the experimental recombination lifetime. The results of the intensity-dependent time-resolved microwave measurements (Fig. 2) are used to calculate the recombination rate per electron-hole pair as in Ref. [21]:

$$R(n) = \frac{1}{\Delta n} \frac{d\Delta n}{dt} = \frac{1}{\Delta n} \frac{d\Delta n}{dS} \frac{dS}{dt}, \quad (3)$$

where S is the microwave signal in the TMR measurement. The results of $1/R(n)$ give the instantaneous lifetime as a function of the excess carrier density at each temperature and when it is fitted to the theoretical lifetime model, the minority-carrier lifetime can be extracted for each temperature. In this approach, the contributions of various recombination mechanisms—i.e., SRH, radiative,

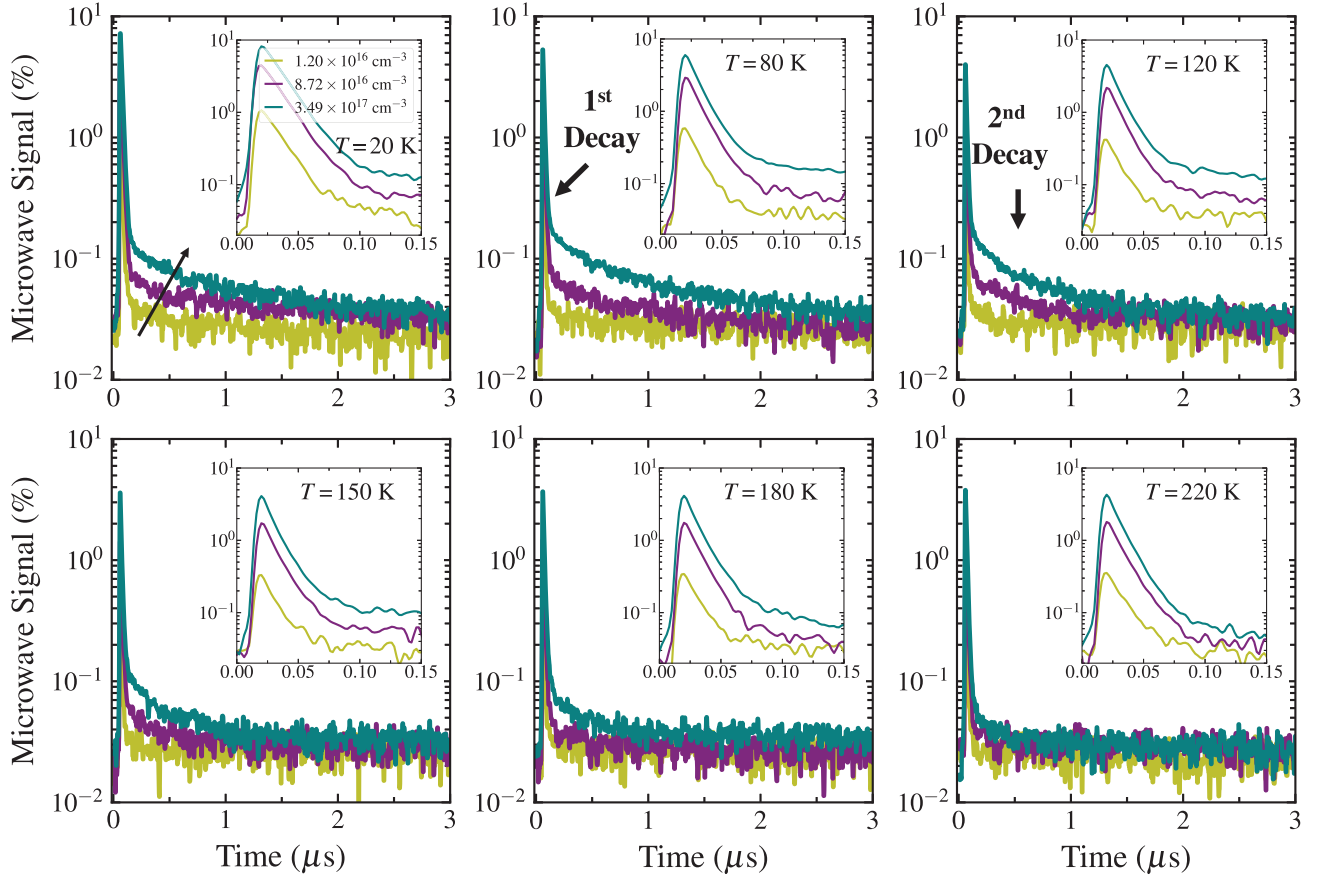


FIG. 2. Time-resolved microwave-reflectance decays are shown for various initial optically generated carrier densities and sample temperatures in the MWIR InAs/GaSb T2SL absorber. The arrows highlight two primary decays. We attribute the first faster decay to the recombination of the minority carriers, which occurs during the first few tens of nanoseconds (inset); the second decay is not usually observed and is currently under investigation.

and Auger recombination—to the total lifetime are determined separately as functions of the temperature and the carrier density.

The common parameters used throughout this analysis are the equilibrium electron (n_0) and hole (p_0) concentrations, the energy gap (E_g), Boltzmann's constant (k_B), the temperature (T), and the effective electron (m_e) and hole (m_h) masses. We determine the energy gap from photoluminescence (PL) spectra of the T2SL absorber as a function of the temperature. Figure 3 shows measured PL spectra for the T2SL absorber for temperatures between 20 and 300 K. The temperature dependence of the band gap, along with the Varshni fitting, is presented in the inset.

B. The theoretical model to calculate the lifetime

The bulk recombination lifetime is determined by the SRH-, radiative-, and Auger-recombination mechanisms as

$$\tau^{-1} = \tau_{\text{SRH}}^{-1} + \tau_{\text{rad}}^{-1} + \tau_{\text{Auger}}^{-1}. \quad (4)$$

We summarize the main expressions for each of these recombination processes in the following.

C. The Shockley-Read-Hall lifetime

The SRH lifetime is due to recombination of the electron-hole pairs through deep-level impurities or traps, with excess energy carried away by lattice vibrations or phonons. It can be characterized by the defect density N_t , the SRH-defect energy levels E_t , and the electron- and hole-defect capture cross sections σ_n and σ_p , respectively, as [22]

$$\tau_{\text{SRH}}^{-1} = \frac{n_0 + p_0 + \Delta n}{\tau_{p_0}(n_0 + n_1 + \Delta n) + \tau_{n_0}(p_0 + p_1 + \Delta p)}. \quad (5)$$

Here, Δn and Δp are the excess carrier densities, taken to be equal in the absence of trapping [23], and n_1 , p_1 , τ_{n_0} , and τ_{p_0} are defined as follows:

$$n_1 = N_c \exp\left(\frac{E_t - E_c}{k_B T}\right), \quad p_1 = N_v \exp\left(\frac{E_v - E_t}{k_B T}\right), \quad (6)$$

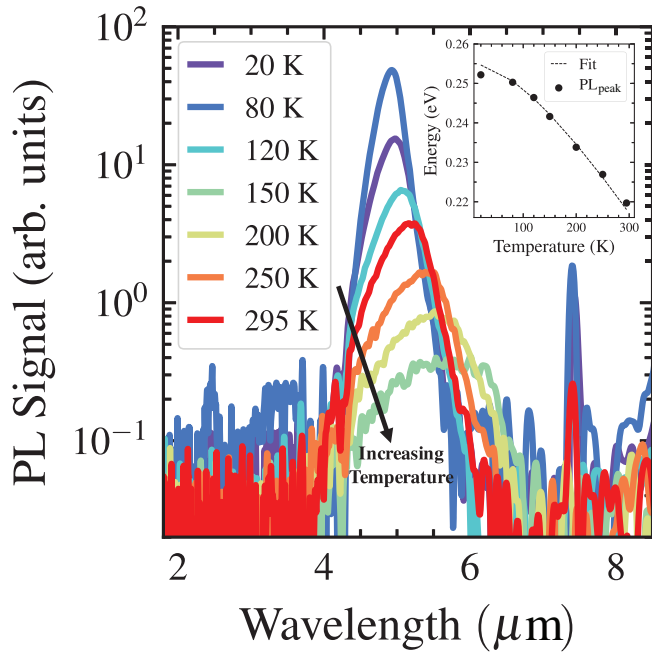


FIG. 3. The measured photoluminescence spectra of the T2SL absorber and the peak PL energy (inset, black circles) as a function of the temperature. The dashed line shows the Varshni fit with parameters $\alpha = 0.24$ meV/K and $\beta = 270$ K.

and

$$\tau_{n_0} = \frac{1}{\sigma_n v_n N_t}, \quad \tau_{p_0} = \frac{1}{\sigma_p v_p N_t}, \quad (7)$$

where v_n and v_p are the electron and hole thermal velocities.

Equation (5) describes the density dependence of SRH recombination, and for a p -type material, i.e., $p_0 \gg n_0$, can be further simplified for low-level injection (LL) ($\Delta n \ll p_0$) and high-level (HL) injection ($\Delta n \gg p_0$) conditions as

$$\begin{aligned} \tau_{\text{SRH}}(\text{LL}) &= \frac{n_1}{p_0} \tau_{p_0} + \left(1 + \frac{p_1}{p_0}\right) \tau_{n_0} \\ &= \tau_{n_0}, \quad \text{for } n_1, p_1 \ll p_0, \end{aligned} \quad (8)$$

and

$$\tau_{\text{SRH}}(\text{HL}) = \tau_{p_0} + \tau_{n_0}, \quad (9)$$

which indicates that the SRH lifetime for p -type material is limited by the minority-electron-recombination lifetime τ_{n_0} for the LL injection regime and is the sum of both carriers' lifetimes for the HL-injection regime.

D. The radiative lifetime

The radiative lifetime is associated with the band-to-band recombination of electron-hole-pairs, in which the

resultant energy is released as photons. The radiative lifetime can be calculated as [24]

$$\tau_{\text{rad}}^{-1} = B(n_0 + p_0 + \Delta n), \quad (10)$$

where B is the radiative-recombination coefficient determined by the superlattice band structure and is related to the microscopic radiative coefficient (B_r) using the photon-recycling factor ($B_r = B\Phi$). Photon recycling trends to unity for thin samples. However, as the thickness of the active layer increases, the contribution of self-absorption followed by electron-hole generation and radiative recombination must be taken into account, which leads to $\Phi > 1$ [25].

Under LL- and HL-injection conditions, Eq. (10) for a p -type material can be written as

$$\tau_{\text{rad}}(\text{LL}) = \frac{1}{Bp_0}, \quad \tau_{\text{rad}}(\text{HL}) = \frac{1}{B\Delta n}. \quad (11)$$

E. The Auger lifetime

The Auger lifetime is a three-carrier process in which an electron-hole-pair recombine and a third carrier absorbs their recombination energy. Depending on the third carrier being either a conduction-band electron or a valence-band hole, the Auger-recombination rate is either proportional to n^2p [for the electron-electron-hole (*eeh*) process] or to p^2n [for the electron-hole-hole (*ehh*) process]. The Auger lifetime can be calculated as [24]

$$\begin{aligned} \tau_{\text{Auger}}^{-1} &= C_n(n_0 + \Delta n)(n_0 + p_0 + \Delta n) \\ &\quad + C_p(p_0 + \Delta n)(n_0 + p_0 + \Delta n), \end{aligned} \quad (12)$$

where C_n and C_p are the Auger coefficients of the *eeh* process and the *ehh* process, respectively. Generally, the *eeh* process is the dominant Auger-recombination mechanism in n -type materials, while for the p -type materials, the hole-dominated *ehh* process involving two holes and an electron should also be considered in addition to the *eeh* process. In the limiting cases of LL- and HL-injection conditions, Eq. (12) leads to

$$\tau_{\text{Auger}}(\text{LL}) = \frac{1}{C_p p_0^2}, \quad \tau_{\text{Auger}}(\text{HL}) = \frac{1}{(C_p + C_n)\Delta n^2}. \quad (13)$$

As can be seen, under LL conditions, τ_{Auger} is injection independent and its magnitude is proportional to the inverse square of the doping concentration, whereas under *hl* conditions, τ_{Auger} decreases as the injection density increases and its magnitude is independent of the doping concentration.

Auger recombination is a strong function of the material's electronic structure and in the case of the superlattices with highly nonparabolic energy bands requires

significant computational resources, which has limited accurate comparison between the experiment and the theoretical calculation. Precise determination of the Auger rate is beyond the scope of the present work and it will suffice to use the analytical expressions by Beattie, Landsberg, and Blakemore (BLB) [26] to obtain an estimate of the temperature-dependent Auger lifetime. For this purpose, the temperature dependence of the *ehh* process for a *p*-type material can be written as [27]

$$\frac{1}{\tau_{\text{Auger}}} = \frac{1}{\tau_{\text{ehh}}} + \frac{1}{\tau_{\text{ehh}}}, \quad (14)$$

where the expressions for τ_{ehh}^{-1} is as follows:

$$\tau_{\text{ehh}}^{-1} = \frac{(n_0 + p_0)n_0}{2n_i^2} (\tau_{\text{ehh}}^i)^{-1}. \quad (15)$$

Here, τ_{ehh}^i is calculated as [28]

$$\tau_{\text{ehh}}^i = \tau_{\text{ehh}}^i(T \rightarrow \infty) \times \exp \left[\left(\frac{1 + 2\mu}{1 + \mu} \right) \left(\frac{E_g}{k_B T} \right) \right], \quad (16)$$

where $\tau_{\text{ehh}}^i(T \rightarrow \infty)$ is unknown and used as a fitting parameter. Similarly to τ_{ehh}^i , the corresponding relation for the *ehh* process is given by

$$\tau_{\text{ehh}}^{-1} = \frac{(n_0 + p_0)p_0}{2n_i^2} (\tau_{\text{ehh}}^i)^{-1}, \quad (17)$$

where τ_{ehh}^i can be calculated using the ratio

$$\gamma = \frac{C_n}{C_p} = \frac{\tau_{\text{ehh}}^i}{\tau_{\text{ehh}}^i}. \quad (18)$$

Considering a *p*-type material, the data of experimental recombination lifetime $1/R(n)$ as a function of the car-

rier density determined from the intensity-dependent TMR measurements are fitted to the total lifetime using Eqs. (4), (5), (10), and (12) as

$$\tau^{-1} = \frac{p_0 + \Delta n}{\tau_{p_0}(\Delta n) + \tau_{n_0}(p_0 + \Delta n)} + B(p_0 + \Delta n) + C_p(p_0 + \Delta n)^2. \quad (19)$$

Figure 4 shows the data (circles) for representative temperatures, compared with the overall fit (solid curve). As τ_{Auger} shows a stronger dependence on the injection level than τ_{rad} , Auger recombination becomes dominant and the contribution of radiative recombination is relatively too small to reliably estimate the radiative coefficient *B*. Therefore, we fit the lifetime using τ_p , τ_n , and C_p as the fitting parameters, neglecting the radiative-recombination process.

The best fits are obtained for C_p values of 5.1×10^{-28} cm⁶/s at 20 K and 3.2×10^{-28} cm⁶/s at 300 K. Previous studies have reported Auger coefficients equal to 1.0×10^{-28} cm⁶/s at 60 K [29] and 1.3×10^{-27} cm⁶/s [30] and 1.1×10^{-27} cm⁶/s at 77 K [31] in Ga-containing superlattices. Furthermore, the results indicate that τ_p is lower than τ_n for temperatures above 50 K and that both decrease gradually with temperature.

Based on Fig. 4, under all the operating temperatures, the low-injection portion of τ_{total} is dominated by SRH recombination, while in the higher-injection regime ($> 1.0 \times 10^{17}$ cm⁻³), the Auger contribution is most significant.

For analysis of the temperature-dependent lifetime, the extracted fitting parameters τ_{n_0} and C_p from above at each temperature are used to measure the minority-carrier lifetime, under the assumption of a LL-injection condition, using

$$\tau_{\text{MC}}^{-1} = \tau_{n_0}^{-1} + C_p p_0^2. \quad (20)$$

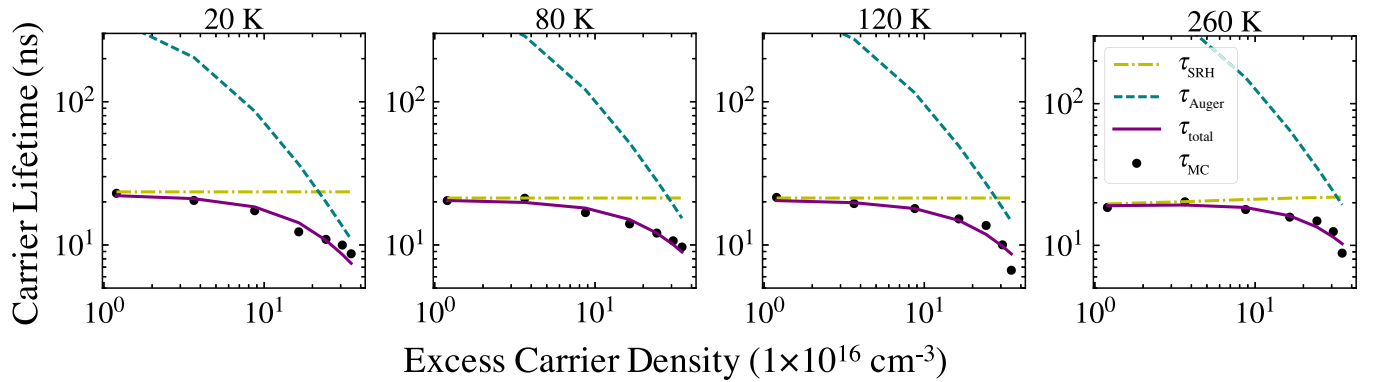


FIG. 4. The measured minority-carrier lifetime as a function of the excess carrier density for a representative subset of temperatures, along with the calculated SRH and Auger-lifetime components. The total lifetime, shown as the solid curve, is the best fit for the measured lifetime to extract different fitting parameters. The radiative-lifetime component has a negligible effect on the total lifetime and is not shown.

Having τ_{MC} values at each measured temperature, we fit the experimental data for temperatures ranging from 20 to 250 K to the theory based on Eqs. (4), (5), and (14), using E_t , $\sigma_n N_t$, p_0 , $\tau_{eeh}^i(T \rightarrow \infty)$, and γ as fitting parameters. For simplicity, we assume σ_p and σ_n to be equal ($=\sigma$) and use the effective masses that we obtain using the Naval Research Laboratory NRL MULTIBANDS[®] software [32]: $m_e = 0.034m_0$ and $m_h = 0.132m_0$.

The best-fitting parameters are found to be $E_t = 5$ meV, $\sigma N_t = 2.4$ cm⁻¹, $p_0 = 1.0 \times 10^{17}$ cm⁻³, and $\tau_{eeh}^i(T \rightarrow \infty) = 9.0 \times 10^{-12}$ s⁻¹ and γ is found to be 18. When the background doping concentration of $p_0 = 5.0 \times 10^{16}$ cm⁻³ from the growth calibration is used as an input in the model, a similar fit is achieved with minor adjustment to all the fitting parameters except for E_t and γ , which change to 9 meV and 5, respectively.

Figure 5 shows the minority-carrier lifetime as a function of the temperature. The results indicate that the lifetime is SRH limited for 80 to 150 K, while Auger recombination is dominant above 150 K. Due to the large doping of the sample, the radiative transition is limited and Auger recombination is leading.

Although the lifetime and the extracted fitting parameters in this work are in close agreement with the previously reported results [20,29,33], it would be helpful to summarize the anticipated sources of error in our measurement, which might pose some uncertainty with regard to the estimated carrier density and hence the extracted lifetime.

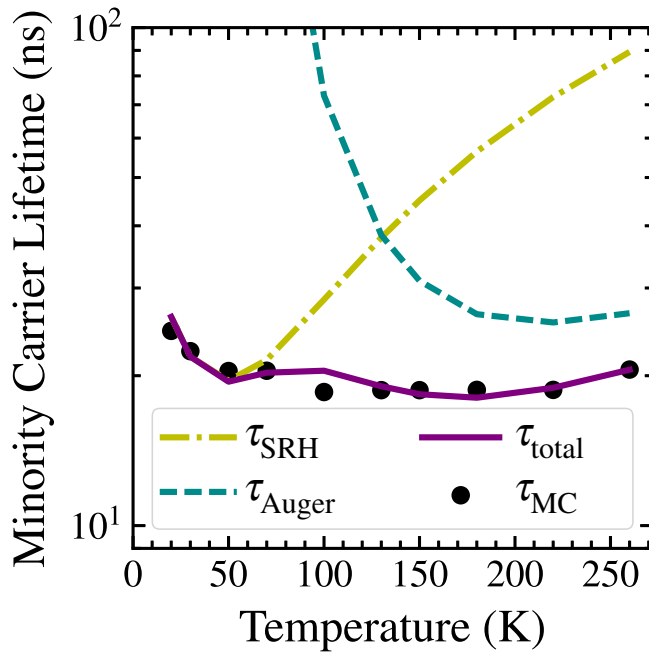


FIG. 5. The temperature-dependent measured minority-carrier lifetimes (black circles), compared to the low-injection-level SRH and Auger-lifetime components. The solid curve is the best fit for the total lifetime to extract different fitting parameters.

There is a lateral gradient in the Gaussian beam profile of the laser illuminated on the sample, which may cause nonuniform injection. Also, there are possible losses in the measurement system, for example, due to the cryostat windows, etc. In addition to possible errors in the determination of the carrier density, the lifetime measurement has a limitation error if time is measured on the order of the minimum response time of the system. Furthermore, the parameters extracted from the fitting procedure are not unique. Therefore, one needs to carefully consider the uncertainty in the fitting procedure in the analysis of the lifetime results.

Having the minority-carrier lifetime as a function of the temperature, the minority-carrier mobility can be calculated versus the temperature, provided that the minority-carrier diffusion length is known. In the following, we utilize EBIC to estimate L_e and, consequently, we calculate the mobility using Eq. (2).

IV. THE DIFFUSION LENGTH

A. EBIC measurement

In EBIC, a beam of high-energy electrons is scanned across a sample containing a p - n junction or a Schottky junction. The beam generates charge carriers through inelastic collisions with the crystal's lattice. The electron-hole pairs diffuse to the junction and are then swept across the depletion region and collected externally through the contacts and measured by a sensitive current amplifier. The result is a spatially resolved map of the sample's current and, when accompanied by analytical models [34], it can be used to determine various transport properties, including the diffusion length. To study the transport characteristics along the growth direction with EBIC, the “normal-collector geometry” configuration is used, in which the plane of the collecting p - n junction is perpendicular to the irradiated surface. For this purpose, the processed sample is cleaved to expose the side walls of the devices. This step is facilitated by reducing the thickness of the substrate before cleaving to achieve a smooth side wall. The prepared devices are wire bonded and mounted on a variable-temperature cold stage cooled by liquid nitrogen inside a JSM-IT100 SEM.

As a result of the e -beam incidence on the side wall of the device at any distance away from the p - n junction, a volume of electron-hole pairs is generated in the sample. Under $||$ injection, carriers will undergo diffusion-based motion across the illuminated region toward the p - n junction and contribute to the total current induced in the junction. The diffusion of minority electrons will dominate the current, since the wide-band-gap hole-barrier layer is engineered to block the flow of majority holes. The electron-induced current at various e -beam positions with respect to the junction [$I_{EBIC}(x)$] is collected using an SR570 current amplifier while the device is held at zero

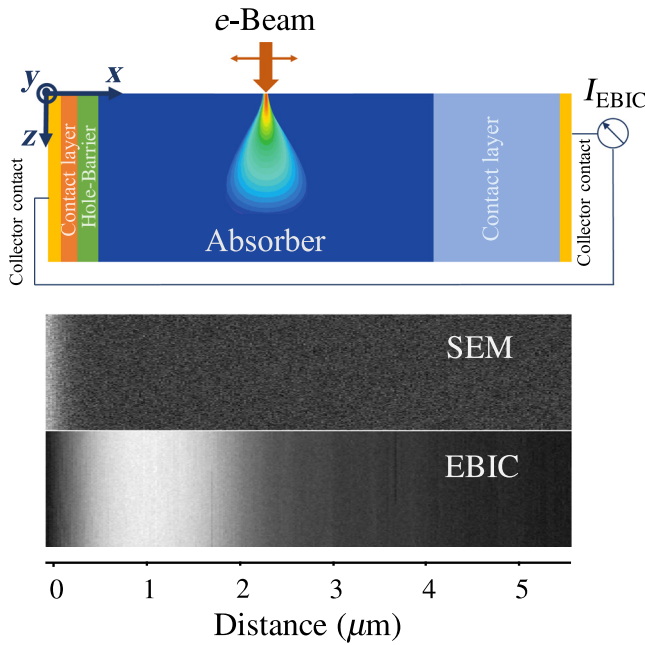


FIG. 6. Top: the structure of the InAs/GaSb nBp T2SL and the generated electron-hole volume in the absorber region due to the e -beam impingement on the sample. Bottom: scanning electron microscopy (SEM) and EBIC images of the cross section of the device under test at an e -beam energy of 20 keV and $T = 80$ K.

bias. Figure 6 (top) illustrates the geometry of the sample in the EBIC setup, including the generation volume due to the e -beam incidence on the absorber region of the sample. Figure 6 (bottom) shows the cross-section SEM and EBIC images from the side wall of the device for 80 K.

Due to the high energy of the electrons in the beam, a single high-energy electron incident on the semiconductor generates a sufficient current. Therefore, careful design of the experiment and measurement setup is required to consider the effect of the excitation level on the transport. Moreover, one should note the effect of the surface in the analysis of the EBIC data. The cleaved surface at the top, where the beam impinges on the sample, and the absorber–bottom contact interface (back surface) can contribute to the surface recombination. The surface-recombination velocity acts as a sink for the generated carriers at these surfaces and its effect, in addition to the influence of various external perturbations (e.g., temperature) has to be taken into consideration in the analysis of the EBIC results. For this purpose, we investigate the dependence of EBIC on the surface recombination, by studying EBIC at varying e -beam energies and currents at temperatures ranging from 80 to 150 K. Figure 7 shows the resultant line-scan profile $I_{EBIC}(x)$ obtained for three representative temperatures for beam currents of 1.5, 3.5, 8.5, and 35 pA, denoted as 10%, 20%, 30%, and 40% of the filament current in the SEM, for a beam energy of 20 keV [Figs. 7(a)–7(c)] and for e -beam energies of 10, 15, and

20 keV for a beam current of 35 pA [Figs. 7(d)–7(f)]. The e -beam current incident on the sample is measured using a Faraday cup.

As can be seen, the collected EBIC signal first rises steeply as the beam moves toward the depletion region and reaches its maximum in the depletion region due to the built-in field, then decays slowly as the e -beam moves further toward the substrate. The roll-offs on either side of the depletion region are relative to the diffusion and recombination characteristics of the minority carriers in each region. We find the n region to be wholly depleted and the depletion region to be extended to the p region (absorber layer), changing with the temperature and the e -beam energies.

We note in Figs. 7(a)–7(c), that with increasing temperature, the EBIC signal decays more slowly. Also, as the e -beam current increases at a fixed temperature, the EBIC signal rises and the falling edge associated with the absorber region becomes steeper. This observation is due to the characteristic of the surface at the top. Unlike bulk recombination, surface recombination depends not only on the density of surface states or interface traps but also on the charge state of surface states, i.e., depletion or accumulation [23]. We believe that the cleaved side wall of the device exposes the narrow-band-gap absorber region to oxide formation and hence acts as an attracting potential for the generated excess carriers. By increasing the injection current, the enhanced density of excess carriers results in the saturation of the surface states; hence, the surface-induced attractive potential for minority carriers vanishes and the surface recombination diminishes and, consequently, the signal due to the diffusion of the carriers rises. In contrast, the interface of the absorber and the bottom contact (back surface) is accompanied by a low surface-recombination velocity in the case of our structure, due to the higher-doped bottom contact with respect to the absorber. The band offset at this interface builds a repulsive potential to minority carriers, which inhibits further recombination.

To shed more light on the surface-recombination current, we also investigate the effect of the beam energy in the SEM. At higher e -beam energies, minority carriers are generated more deeply and, hence, are less likely to diffuse to the surface and recombine there. While at lower e -beam energies, the collection process is controlled by the collection probability at the surface of the sample and the surface-recombination velocity influences the current profile. As can be seen in Fig. 7(d)–7(f), higher beam energies give not only broader carrier generation distribution but also significantly higher carrier concentrations, so more carriers are collected and, consequently, the signal increases.

Here, we report the minority-carrier diffusion length for the electron current of 40% (35 pA), for which surface recombination is negligible, and the beam energies of 10,

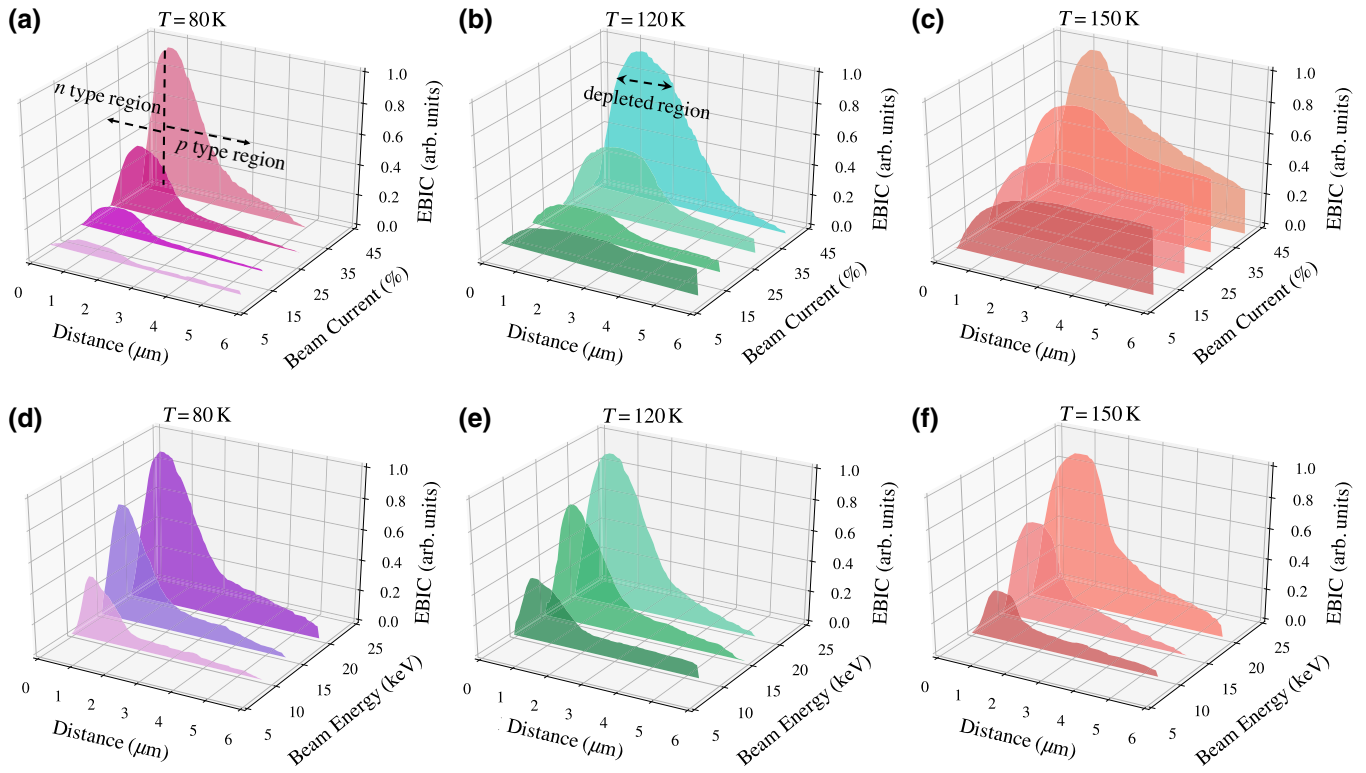


FIG. 7. Experimental EBIC data are shown for three representative temperatures of 80, 120, and 150 K with (top) a varying beam current, denoted as the percentage of the total filament current in the SEM, for a 20 keV beam energy and (bottom) a varying beam energy in kilo electron volts at a beam current of 35 pA. The EBIC intensities are normalized by the signal peak maximum at the highest current (top) and accelerating voltage (bottom). The n , p , and depleted regions associated with each part of the EBIC signal are shown in (a) and (b).

15, and 20 keV. In the following, we briefly explain the semiparametric model used to extract the diffusion length from the EBIC data.

B. The theoretical model

Various models have been reported previously to provide an acceptable first-order prediction of EBIC data [34–36]. Here, we use the model proposed by Bonard and Ganière [34]. This model, which will be referred to as Bonard’s model in this paper, can be considered as the generalized form of an earlier model by Donolato [35]. Bonard’s model accounts for the contribution of all three regions of a p - n junction—i.e., the n -type region, the depletion region, and the p -type region—in the EBIC signal, while considering the surface recombination at the top surface, for the case of the extended source.

We fit the experimental EBIC data to analytical expressions for the carrier collection efficiency to extract the vertical minority-carrier diffusion length, with the diffusion length (L_e) and the ratio of the surface-recombination velocity to the diffusion coefficient (S_e/D_e) as fitting parameters. The charge-collection efficiency $\eta(x)$ is $I_{\text{EBIC}}(x)$, normalized to the total number of generated

electron-hole pairs G_0 . Then $\eta(x)$ can be calculated from the convolution of two terms: the probability of collection $\phi(x, z)$, defined as the likelihood of a carrier being collected and contributing to the EBIC current after diffusion, and the generation function $h(x, z)$ as [34]

$$\eta(x) = \int_{-\infty}^{+\infty} dx' \int_0^{+\infty} h(x' - x, z') \Phi(x', z') dz'. \quad (21)$$

The translational symmetry along the y direction (specified in Fig. 4) reduces the problem to a 2D configuration. Hence the integral is calculated over the generation volume on the x - z plane.

The spatial distribution of the minority carriers can be defined as [34]

$$h(x, z) = \frac{1}{a} \exp\left(-\frac{x^2}{\sigma_x^2}\right) z^2 \exp\left(-\frac{z}{\sigma_z}\right) dx dz, \quad (22)$$

where σ_x is the lateral electron range and σ_z is the depth electron range, these being dependent on the material and the beam parameters. The accuracy of the model is highly dependent on the calculated generation distribution, so

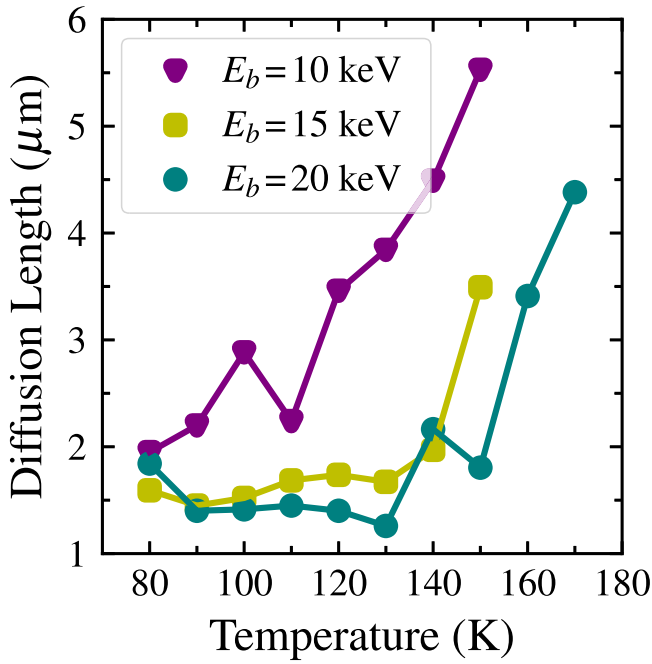


FIG. 8. Extracted minority-carrier diffusion lengths (L_e) for an InAs/GaSb nBp MWIR sample as a function of the temperature. The minority-carrier diffusion lengths are extracted from the EBIC line-scan profiles for e -beam energies of 10, 15, and 20 keV and an e -beam current of 35 pA.

more realistic models such as the Monte Carlo SEM interaction simulator Casino [37] are usually used to calculate the spatial distribution of generated electron-hole carriers in the material. The normalized distribution of the electron-hole pairs from Monte Carlo simulation is then used to extract σ_x and σ_z by fitting the numerical results to Eq. (21), as a function of the beam spot size and the beam energy [38]. Finally, the obtained generation function is used along the calculated $\phi(x, z)$ for each region of the photodiode, as described previously [11].

We repeat our measurements several times for each e -beam current and energy and extract the L_e using the aforementioned model. Caution should be exercised in fitting theoretical curves to the experimental data, since equally good agreement can often be obtained for several combinations of material parameters. The results of L_e for variable e -beam current values at the beam energies of 10, 15, and 20 keV are presented in Fig. 8.

V. DISCUSSION

Figure 8 shows the extracted minority-carrier diffusion length for three e -beam energies of 10, 15, and 20 keV at a beam current of 35.5 pA. The results for $E_b = 15$ and 20 keV show similar trends with the temperature, while the 10 keV data are different and show higher values for L_e . As mentioned above, the e -beam energy defines the depth of the generation volume in EBIC and minority carriers

generated closer to the surface at lower E_b are more likely to contribute to the surface current rather than diffuse and be collected through the depletion region. From this perspective, we believe that the behavior at 10 keV is due to the surface effect.

On the other hand, we see that the values for the diffusion length at 15 and 20 keV are very low and have a low-temperature dependency up to 140 K, after which they increase. For the temperature range of 80–140 K, the diffusion length is found to be about $1.5 \mu\text{m}$ for an absorber thickness of $4 \mu\text{m}$. It should be noted that based on the EBIC data in this temperature range, the depleted region is extended by about $0.7 \mu\text{m}$ into the absorber, which makes the required travel distance less for the carrier. This might explain the high quantum efficiency reported previously on the same structure [16].

Now that we have the minority diffusion length and the lifetime at each temperature, μ_e is calculated at various operating temperatures using Eq. (1). Figure 9 shows the results of the minority-carrier mobility against the temperature for the three e -beam energies. Since the lifetime is found to have a minor dependency in the range of 80–150 K, the general trend of μ_e follows the pattern of the extracted L_e , which is fairly independent of the temperature up to 140 K, for e -beam energies of 15 and 20 keV, and increases linearly beyond that.

In order to understand the observed mobility trend, one needs to consider different limiting factors. In the

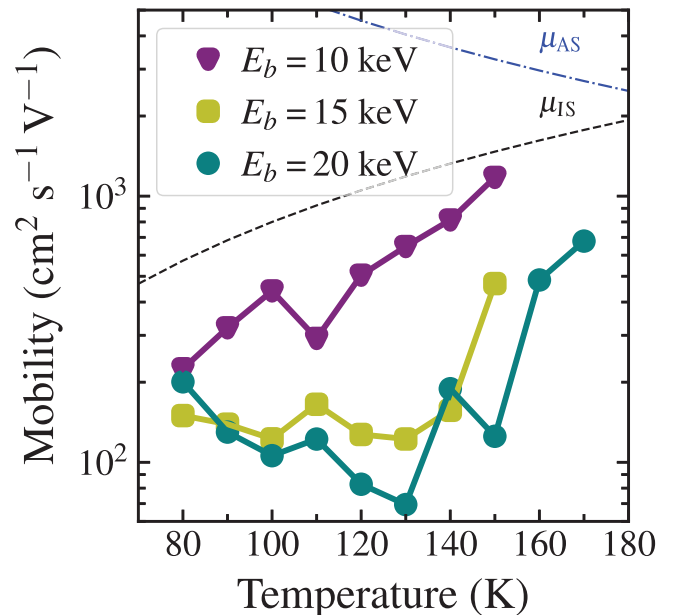


FIG. 9. The vertical electron mobility for a InAs/GaSb nBp MWIR sample as a function of the temperature for e -beam energies of 10, 15, and 20 keV, obtained using the extracted diffusion length and the minority-carrier lifetime from EBIC and TMR measurements, respectively.

semiclassical study of transport in superlattices, disorders such as structural and phonon-induced disorders are responsible for destroying the long-range coherence of the electron states and, as a result, lead to localization through different scattering mechanisms, such as phonon-induced scattering, ionized impurity scattering, and interface roughness scattering (IRS). However, none of these scattering mechanisms can be accountable for the observed trend in the electron mobility data as shown in Fig. 9. Each of these scattering mechanisms has a different temperature dependency [6]: the impurity scattering is most effective at lower temperatures, with the mobility μ_{IS} having a roughly $T^{3/2}$ dependency on the temperature, while at higher temperatures, phonon scattering dominates and the mobility μ_{AS} is approximately $T^{-3/2}$. These trends are shown in Fig. 9 for comparison. On the other hand, IRS can happen due to growth imperfections, such as microscopic fluctuation of the composition of constituent layers, which can lead to the degradation of electron mobility. However, the effect of IRS tends to increase weakly with decreasing temperature [39].

The trend in the mobility can be explained separately for two temperature regions of 80–140 K (region 1) and above 140 K (region 2). For region 1, we believe that the transport is limited by trap-assisted transport rather than miniband conduction, due to the presence of the deep-level states. In a perfectly periodic crystal, the charge density spreads uniformly throughout the crystal and the only states are those described by Bloch waves [4], while in the presence of localized imperfections, energy states appear within the forbidden gaps, the wave functions of which are localized in the vicinity of the impurity. The carriers that are bound to the impurity are not free to move anywhere in the crystal. The minority-electron mobility is controlled by the extent to which they can be released from these bound impurity states [28]. In region 2, the increase in the mobility with the temperature can be associated with the carriers being set free from the impurity states, with an activation energy of 115 meV. A similar observation has been reported previously in *n*-type InAs/In(As,Sb) T2SL structures [40], in which the results show that above 120 K, the minority-carrier hole transport occurs through minibands, while for lower temperatures, the holes are localized and transport is only due to phonon-assisted tunneling.

VI. CONCLUSION

In summary, we study the vertical minority-electron transport properties in *nBp* MWIR detectors with *p*-type InAs/GaSb absorbers. In order to investigate the transport, the temperature-dependent EBIC measurements are combined with microwave reflectance measurements of minority-carrier lifetimes in the same device, to determine

the vertical electron mobilities from 80 to 150 K. The calculated electron mobility shows two distinct regions. At lower temperatures, the mobility has a weak temperature dependence and its behavior is attributed to carrier localization in deep-level traps. The second region, at higher temperatures, shows an increase with temperature, from which the activation energy of 115 meV is extracted. In addition, we investigate the various recombination mechanisms and determine the limiting mechanisms as a function of the temperature and the excess density. The results show that the lifetime has a minimal temperature dependence and is SRH limited for 80–150 K, while Auger recombination is dominant above 150 K. Furthermore, the effects of different parameters in the EBIC measurements are investigated. The results indicate that the contribution of the surface current on the transport is minimized at higher *e*-beam energies and currents.

ACKNOWLEDGMENTS

This work was sponsored by the Army Research Office (ARO) under Contract No. W911NF-16-2-0068 and by the Air-Force Research Laboratories (AFRL) in response to Contract No. FA9453-14-1-0248. Furthermore, we thank the Naval Research Laboratory (NRL) for providing the use of the NRL MULTIBAND[®] software for device modeling. We also acknowledge the fruitful discussions with Dr. Sergey Maximenco and Dr. Edward Aifer from the Naval Research Laboratories and with Dr. Eric Shaner of Sandia National Laboratories.

-
- [1] A. Rogalski, P. Martyniuk, and M. Kopytko, InAs/GaSb type-II superlattice infrared detectors: Future prospect, *Appl. Phys. Rev.* **4**, 031304 (2017).
 - [2] L. Höglund, R. Marcks Von Würtemberg, C. Asplund, H. Kataria, A. Gamfeldt, and E. Costard, T2SL production and development at IRnova: From MWIR to VLWIR detection, *Infrared Tech. App.* **XLIII** 10177, 1017713 (2017).
 - [3] O. Neshor and P. C. Klipstein, High-performance IR detectors at SCD present and future, *Opto Electron. Rev.* **14**, 59 (2006).
 - [4] H. T. Grahn, *Semiconductor Superlattices: Growth and Electronic Properties* (World Scientific, Singapore, 1995).
 - [5] M. A. Kinch, HgCdTe: Recent trends in the ultimate IR semiconductor, *J. Electron. Mat.* **39**, 1043 (2010).
 - [6] D. A. Neamen, *Semiconductor Physics and Devices* (McGraw-Hill, New York, 2012).
 - [7] G. A. Umana-Membreno, B. Klein, H. Kala, J. Antoszewski, N. Gautam, M. N. Kuttly, E. Plis, S. Krishna, and L. Faraone, Vertical minority carrier electron transport in *p*-type InAs/GaSb type-II superlattices, *Appl. Phys. Lett.* **101**, 1 (2012).
 - [8] B. V. Olson, L. M. Murray, J. P. Prineas, M. E. Flatté, J. T. Olesberg, and T. F. Boggess, All-optical measurement of vertical charge carrier transport in mid-wave infrared

- InAs/GaSb type-II superlattices, *Appl. Phys. Lett.* **102**, 202101 (2013).
- [9] J. V. Li, S. L. Chuang, E. M. Jackson, and E. Aifer, Minority carrier diffusion length and lifetime for electrons in a type-II InAs/GaSb superlattice photodiode, *Appl. Phys. Lett.* **85**, 1984 (2004).
- [10] D. Zuo, R. Liu, D. Wasserman, J. Mabon, Z. Y. He, S. Liu, Y. H. Zhang, Emil A. Kadlec, Benjamin V. Olson, and Eric A. Shaner, Direct minority carrier transport characterization of InAs/InAsSb superlattice nBn photodetectors, *Appl. Phys. Lett.* **106**, 071107 (2015).
- [11] N. Yoon, C. J. Reyner, G. Ariyawansa, J. M. Duran, J. E. Scheihing, J. Mabon, and D. Wasserman, Modified electron beam induced current technique for in(Ga)As/InAsSb superlattice infrared detectors, *J. Appl. Phys.* **122**, 074503 (2017).
- [12] J. Lee, C. J. Fredricksen, E. Flitsiyan, R. E. Peale, Le Chernyak, Z. Taghipour, L. Casias, A. Kazemi, S. Krishna, and S. Myers, Impact of temperature and gamma radiation on electron diffusion length and mobility in *p*-type InAs/GaSb superlattices, *J. Appl. Phys.* **123**, 235104 (2018).
- [13] Z. Taghipour, A. Kazemi, S. Myers, P. S. Wijewarnasuriya, S. Mathews, E. Steenbergen, C. P. Morath, V. M. Cowan, G. Ariyawansa, J. Scheihing, and S. Krishna, Extraction of minority carrier diffusion length of MWIR Type-II superlattice *nBp* detector, *Infrared Sens. Dev. App. VII* **10404**, 6 (2017).
- [14] S. P. Svensson, D. Donetsky, D. Wang, H. Hier, F. J. Crowne, and G. Belenky, Growth of type II strained layer superlattice, bulk InAs and GaSb materials for minority lifetime characterization, *J. Crystal Growth* **334**, 103 (2011).
- [15] P. Martyniuk, M. Kopytko, and A. Rogalski, Barrier infrared detectors, *Opto Electron. Rev.* **22**, 127 (2014).
- [16] A. Kazemi, S. Myers, Z. Taghipour, S. Mathews, T. Schuler-Sandy, S. Lee, V. M. Cowan, E. Garduno, E. Steenbergen, C. Morath, G. Ariyawansa, J. Scheihing, and S. Krishna, Mid-wavelength infrared unipolar nBp superlattice photodetector, *Infrared Phys.* **88**, 114 (2018).
- [17] S. Maimon and G. W. Wicks, nBn detector, an infrared detector with reduced dark current and higher operating temperature, *Appl. Phys. Lett.* **89**, 151109 (2006).
- [18] P. Klipstein, "XBn" barrier photodetectors for high sensitivity and high operating temperature infrared sensors, *Proc. SPIE* **6940**, 69402U (2008).
- [19] J. F. Klem, J. K. Kim, M. J. Cich, S. D. Hawkins, T. R. Fortune, and J. L. Rienstra, Comparison of nBn and nBp mid-wave barrier infrared photodetectors, *Quant. Sens. Nanophotonic Dev. VII* **7608**, 76081P (2010).
- [20] L. Höglund, A. Soibel, D. Z. Ting, A. Khoshakhlagh, C. J. Hill, and S. D. Gunapala, Minority carrier lifetime and photoluminescence studies of antimony-based superlattices, *Proc. SPIE* **8511**, 851106 (2013).
- [21] M. E. Flatté, C. H. Grein, T. C. Hasenberg, S. A. Anson, D. J. Jang, J. T. Olesberg, and T. F. Boggess, Carrier recombination rates in narrow-gap InAs/Ga_{1-x}In_xSb-based superlattices, *Phys. Rev. B* **59**, 5745 (1999).
- [22] R. N. Hall, Electron-hole recombination in germanium, *Phys. Rev.* **87**, 387 (1952).
- [23] D. K. Schroder, Carrier Lifetimes in Silicon, *IEEE Transactions on Electron Dev.* **44**, 160 (1997).
- [24] S. Rein, *Lifetime Spectroscopy: A Method of Defect Characterization in Silicon for Photovoltaic Applications* (Springer, Berlin, 2005).
- [25] L. Höglund, D. Z. Ting, A. Soibel, A. Fisher, A. Khoshakhlagh, C. J. Hill, S. Keo, and S. D. Gunapala, Minority carrier lifetime in mid-wavelength infrared InAs/InAsSb superlattices: Photon recycling and the role of radiative and Shockley-Read-Hall recombination mechanisms, *Appl. Phys. Lett.* **105**, 193510 (2014).
- [26] A. R. Beattie and P. T Landsberg, Auger effect in semiconductor, *Proc. R. Soc.* **249**, 16 (1959).
- [27] V. C. Lopes, A. J. Syllaios, and M. C. Chen, Minority carrier lifetime in mercury cadmium telluride, *Semi. Sci. Tech.* **8**, 824 (1993).
- [28] J. Blakemore, *Semiconductor Statistics* (Dover Publications, Inc., Mineola, N.Y., 1962).
- [29] B. C. Connelly, G. D. Metcalfe, H. Shen, and M. Wraback, Direct minority carrier lifetime measurements and recombination mechanisms in long-wave infrared type II superlattices using time-resolved photoluminescence, *Appl. Phys. Lett.* **97**, 251117 (2010).
- [30] E. R. Youngdale, J. R. Meyer, C. A. Hoffman, F. J. Bartoli, C. H. Grein, P. M. Young, H. Ehrenreich, R. H. Miles, and D. H. Chow, Auger lifetime enhancement in InAs – Ga_{1-x}In_xSb superlattices, *Appl. Phys. Lett.* **64**, 3160 (1994).
- [31] J. R. Meyer, C. L. Felix, W. W. Bewley, I. Vurgaftman, E. H. Aifer, L. J. Olafsen, J. R. Lindle, C. A. Hoffman, M. J. Yang, B. R. Bennett, B. V. Shanabrook, H. Lee, C. H. Lin, S. S. Pei, and R. H. Miles, Auger coefficients in type-II InAs/Ga_{1-x}In_xSb quantum wells, *Appl. Phys. Lett.* **73**, 2857 (1998).
- [32] M. P. Lumb, I. Vurgaftman, C. A. Affouda, J. R. Meyer, E. H. Aifer, and R. J. Walters, in *Next Generation (Nano) Photonic and Cell Technologies for Solar Energy Conversion III*, edited by Loucas Tsakalagos (International Society for Optics and Photonics, 2012), Vol. 8471, p. 84710A.
- [33] D. Donetsky, S. P. Svensson, L. E. Vorobjev, and G. Belenky, Carrier lifetime measurements in short-period InAs/GaSb strained-layer superlattice structures, *Appl. Phys. Lett.* **95**, 212104 (2009).
- [34] J. M. Bonard and J. D. Ganière, Quantitative analysis of electron beam induced current profiles across pn junctions in GaAs/Al_{0.4}Ga_{0.6}As heterostructures, *J. Appl. Phys.* **79**, 6987 (1996).
- [35] C. Donolato, Reciprocity theorem for charge collection by a surface with finite collection velocity: Application to grain boundaries, *J. Appl. Phys.* **76**, 959 (1994).
- [36] K. L. Luke, Determination of diffusion length in samples of diffusion-length size or smaller and with arbitrary top and back surface recombination velocities, *J. Appl. Phys.* **90**, 3413 (2001).
- [37] H. Demers, N. Poirier-Demers, A. R. Couture, D. Joly, M. Guilmain, N. De Jonge, and D. Drouin, Three-dimensional electron microscopy simulation with the Casino Monte Carlo software, *Scanning* **33**, 135 (2011).

- [38] C. M. Parish and P. E. Russell, On the use of Monte Carlo modeling in the mathematical analysis of scanning electron microscopy-electron beam induced current data, *Appl. Phys. Lett.* **89**, 192108 (2006).
- [39] F. Szmulowicz, H. J. Haugan, S. Elhamri, and G. J. Brown, Calculation of vertical and horizontal mobilities in InAs/GaSb superlattices, *Phys. Rev. B* **84**, 155307 (2011).
- [40] B. V. Olson, J. F. Klem, E. A. Kadlec, J. K. Kim, M. D. Goldflam, S. D. Hawkins, A. Tauke-Pedretti, W. T. Coon, T. R. Fortune, E. A. Shaner, and M. E. Flatté, Vertical Hole Transport and Carrier Localization in InAs/InAs_{1-x}Sb_x Type-II Superlattice Heterojunction Bipolar Transistors, *Phys. Rev. Appl.* **7**, 024016 (2017).